Role of oxygen vacancies on the structure and density of states of iron-doped zirconia

Davide Sangalli, Alessio Lamperti, Elena Cianci, Roberta Ciprian, Michele Perego, and Alberto Debernardi
Laboratorio MDM - IMM - CNR via C. Olivetti 2, I-20864 Agrate Brianza (MB), Italy
(Received 20 November 2012; revised manuscript received 21 January 2013; published 26 February 2013)

In this paper, we study the effect of iron doping in zirconia using both theoretical and experimental approaches. Combining density functional theory (DFT) simulations with the experimental characterization of thin films, we show that iron is in the Fe^{3+} oxidation state and, accordingly, the films are rich in oxygen vacancies ($V_O^{\bullet\bullet}$). $V_O^{\bullet\bullet}$ favor the formation of the tetragonal phase in doped zirconia (ZrO_2:Fe) and affect the density of states at the Fermi level as well as the local magnetization of Fe atoms. We also show that the Fe($2p$) and Fe($3p$) energy levels can be used as a marker for the presence of vacancies in the doped system. In particular, the computed position of the Fe($3p$) peak is strongly sensitive to the $V_O^{\bullet\bullet}$ to Fe atoms ratio. A comparison of the theoretical and experimental Fe($3p$) peak positions suggests that in our films this ratio is close to 0.5. Besides the interest in the material by itself, ZrO_2:Fe constitutes a test case for the application of DFT on transition metals embedded in oxides. In ZrO_2:Fe, the inclusion of the Hubbard U correction significantly changes the electronic properties of the system. However, the inclusion of this correction, at least for the value $U = 3.3$ eV chosen in the present work, worsen the agreement with the measured photoemission valence band spectra.

DOI: 10.1103/PhysRevB.87.085206 PACS number(s): 75.50.Pp, 68.55.Ln, 71.15.Mb

I. INTRODUCTION

In dilute magnetic semiconductors (DMS), magnetic impurities, usually transition metals (TM), are introduced to produce a magnetic ground state. These systems have been extensively investigated since the discovery of carrier induced ferromagnetism in (In,Mn)As (see Ref. 1) and (Ga,Mn)As (see Ref. 2) and are believed to be fundamental to fabricate spin-based electronic devices. The understanding of DMS physical properties constitutes a challenge for the theory as the fundamental mechanism leading to ferromagnetic interaction can be hardly explained.[3] Also, experimentally, the inclusion and the influence of TM doping is not clearly understood. Indeed, while several DMS were predicted to have a Curie temperature (T_c) above room temperature, no experimental report of $T_c > 300$ K has been left unchallenged by other studies.[4] Moreover, some results suggest that magnetic impurities, at least at very low doping concentration, act as paramagnetic centers.[5] Recently, a new class of DMS, based on oxides such as zirconia (ZrO_2) and hafnia (HfO_2), has received great attention, after the experimental reports of room temperature magnetism in Fe doped HfO_2 and ZrO_2[6–11] and the theoretical prediction of high T_c in TM doped ZrO_2.[12,13]

For a better understanding of the magnetic properties of the system, a clear picture of its structural and electronic properties is fundamental. As opposite to standard bulk materials, where usually the most stable configuration can be unequivocally identified, in DMS the inclusion of the dopant can induce stress, disorder, and defects in the system with many possible configurations close in energy. From one side, theoretically, the modeling of the material, also at the first-principles levels, requires some assumptions on the initial structure and on the position occupied by the dopant. From the other side, experimentally, stress, disorder, and defects make difficult to provide a unique interpretation to the features observed. Thus a combined approach is the best option.

Among the structural defects of dilute magnetic oxides (DMO), oxygen vacancies ($V_O^{\bullet\bullet}$) are believed to affect the magnetism.[8,9,14] Indeed, it has been suggested that delocalized electrons, associated with $V_O^{\bullet\bullet}$, can play a crucial role in the magnetization mechanisms of DMO.[3] However, in this model, $V_O^{\bullet\bullet}$ are assumed to always induce delocalized states, which can mediate the magnetic interaction. This assumption is true in the undoped oxide, while in presence of doping should be verified case by case.

In the present paper, we describe the structural and electronic properties of iron-doped zirconia (ZrO_2:Fe) focusing our attention on the role of $V_O^{\bullet\bullet}$ and on their relation with the dopant. The role of $V_O^{\bullet\bullet}$ in ZrO_2:Fe and, in general, in ZrO_2 doped with valence $+3$ elements (X^{+3}, with $X =$ Fe,Y, etc.) has been, in part, explored in view of different applications, for oxygen sensing[15–17] and more recently for resistive switching memories.[18,19] For ZrO_2:Fe, in particular, only few experimental reports exist. Also for TM doped oxides, in general, no systematic theoretical description of the relation between $V_O^{\bullet\bullet}$ and doping exist. For example, the $V_O^{\bullet\bullet}$ formation energy, in presence of doping, is usually considered[18] only for the $V_O^{\bullet\bullet}$ to dopant atoms ratio, $y_{V_O^{\bullet\bullet}/X}$, equal to 1, and again, $V_O^{\bullet\bullet}$ are assumed to induce delocalized states, which could mediate the electron conduction in case of resistive switching, regardless of the value of $y_{V_O^{\bullet\bullet}/X}$.

Instead, in case of X^{+3} elements, like iron, the most stable configuration is expected to have $y_{V_O^{\bullet\bullet}/X} = 0.5$ for charge compensation.[20] We thus focus our attention on this configuration describing how the properties of the system would change if $y_{V_O^{\bullet\bullet}/X}$ deviates from the value 0.5.

In Sec. II, we describe both the theoretical and the experimental approaches to the description of ZrO_2:Fe. The results from first-principles simulations are presented in Sec. III. The electronic and structural properties of the system are described as a function of the doping and oxygen vacancies concentration within density functional theory (DFT) in the standard generalized gradient approximation (GGA). For TM oxides, the standard approximations to DFT are known to fail in the description of the so-called on-site correlation. Thus DFT can be corrected with a "Hubbard" term, DFT + U scheme, where U is an external parameter, which improves the

DOS of the valence electrons. However, little is known in the case of TM used as dopant in DMO. Thus we also investigate how this term would influence the electronic properties of the system in ZrO_2:Fe.

The experimental results are then presented in Sec. IV. Here we show that, indeed, the measured properties best agree with the $y_{V_O^{\bullet\bullet}/X} = 0.5$ configuration. Moreover, a detailed comparison of the measured valence band (VB) and DFT density of states (DOS) is done. This is a direct way to explore the value of the on-site electronic correlation on this system, i.e., to adjust the value of the U parameter to be used in the DFT + U approach.

II. FRAMEWORK

A. Computational approach

We computed, from first-principles, the ground state of the two most common phases of ZrO_2, i.e., the tetragonal and the monoclinic phases, at different doping concentrations. We used the PWSCF (4.3.2) package,[21] considering a supercell with 96 atoms (few less when $V_O^{\bullet\bullet}$ are considered) and in some cases, also a smaller supercell with 12 atoms for the description of the highest doping configuration. For all systems, the atomic positions are fully relaxed. The ground state was computed within the GGA[22] to the DFT scheme[23,24] with ultrasoft pseudopotentials.[25,26] We used a 35 Ry cutoff for the wave functions, 400 Ry cutoff for the augmentation density and a Monkhorst-Pack grid $2 \times 2 \times 2$ for the Brillouin zone to have the error on the energy differences between the monoclinic and the tetragonal phase lower than 1 meV per formula unit (f.u.); this was the most stringent condition for our simulations. We estimated the error on the total energy to be lower than 0.1 eV/f.u. Convergence parameters are 10^{-8} Ry on the total energy for the scf cycles and both 10^{-4} Ry on the total energy and 10^{-3} Ry/Bohr on the forces for the atomic relaxation. The pseudopotential of Zr includes semicore electrons. Fe atoms were placed at the substitutional Zr sites and kept as far as possible from each other to mimic uniform doping. For $V_O^{\bullet\bullet}$, instead we considered many different configurations (see discussion in Sec. III), specifically, we considered ZrO_2:Fe at the atomic doping concentration $x_{Fe} = 6.25\%$, 12.5%, 18.75%, 25% with, $y_{V_O^{\bullet\bullet}/Fe} = 0.5$, and without, $y_{V_O^{\bullet\bullet}/Fe} = 0$, oxygen vacancies. We also considered $y_{V_O^{\bullet\bullet}/Fe} = 1.0$ for $x_{Fe} = 6.25\%$, 25%. In total, we studied about 50 different systems of $Zr_{1-x}Fe_xO_{2-z}V_{O_z}^{\bullet\bullet}$ changing x_{Fe} and $z_{V_O^{\bullet\bullet}} = x_{Fe} \times y_{V_O^{\bullet\bullet}/Fe}$ for either the monoclinic or the tetragonal structure. For few selected configurations, i.e., at the lowest and the highest considered doping concentrations $x_{Fe} = 6.25$, 25%, we also performed calculations within the simplified GGA + U approach[44] implemented in the PWSCF package, again considering $y_{V_O^{\bullet\bullet}/Fe} = 0$, 0.5, 1, in order to explore the effect of the Hubbard correction on the electronic structure of the system. The results are presented mainly for the high-doping situation, which we have also investigated experimentally. The configurations at $y_{V_O^{\bullet\bullet}/Fe} = 0$ and 1 resulted to be metallic and in this case the convergence of the physical quantities against the sampling of the k-points grid was verified.

The cell parameters for both the tetragonal and the monoclinic phase of pure ZrO_2 are the same used in Ref. 31. Specifically for the monoclinic phase $a = 5.18$ Å, $b/a = 1.011$, $c/a = 1.037$, and $\beta = 99°10'$, while for the tetragonal phase $a = 5.18$ Å and $c/a = 1.0305$. The same parameters were used for ZrO_2:Fe as well. However, we even performed a full relaxation of our 96 atoms supercell for few selected configurations, and we found out that this has a negligible impact on the properties of the system here considered.

In Sec. III, we systematically compare the results of the present simulations with the ZrO_2:Y (Y doped ZrO_2) system. Yttrium is one of the most studied and used dopants of ZrO_2 and shares with iron the same valence. All the data reported for ZrO_2:Y are from Ref. 31.

In order to describe the semicore levels of iron and compare the results with XPS measurements, we run calculations with a norm-conserving fully-relativistic approach. To this end, we used Hartwigsen, Goedecker, and Hutte (HGH) pseudopotentials,[27] which contain semicore electrons in valence and are constructed with a fully relativistic calculation. The latter are not available within the PWscf[21] code and so we used ABINIT(6.8) code.[28] We studied the semicore levels only for the $x_{Fe} = 25\%$ at. case, again considering $y_{V_O^{\bullet\bullet}/Fe} = 0$, 0.5, 1. We used smaller supercells, 12 atoms ($y_{V_O^{\bullet\bullet}/Fe} = 0$ and 1) and a 24 atoms supercell ($y_{V_O^{\bullet\bullet}/Fe} = 0.5$), with cutoff of 170 Ry and a Monkhorst-Pack grid $3 \times 3 \times 3$ and $3 \times 3 \times 2$, respectively, for the Brillouin zone to have the error on the energy levels position lower then 0.1 eV. The very high-energy cutoff was needed, as the norm-conserving HGH pseudopotentials are harder than the ultrasoft ones used with PWscf and also because the semicore levels are much more localized than valence electrons. The value $x_{Fe} = 25\%$ at. was chosen to have smaller supercells but also because this is quite close to the experimentally measured doping concentration in our films. The atomic positions instead were obtained relaxing the same structures with the PWSCF code and then we checked that the residual forces on the atoms computed with ABINIT were negligible.

Finally, for a quantitative comparison of the measured photoemission and the computed VB, we have performed calculations within GGA + U at $U = 1.0$, 2.0, 3.3 eV at $x_{Fe} = 18.75\%$ at. and $y_{V_O^{\bullet\bullet}/Fe} = 0.5$. A theoretical smearing of 0.02 Ry was used to generate the DOS used in Figs. 3 and 4, while a higher smearing of 0.06 Ry was used for the DOS in Fig. 7 to mimic the experimental peak width.

B. Experimental setup

Experimentally ZrO_2 and ZrO_2:Fe thin films were grown on Si/SiO_2 substrates in a flow–type hot wall atomic layer deposition reactor (ASM F120) starting from β-diketonates metalorganic precursors, namely $Zr(C_{11}H_{19}O_2)_4$ for Zr and $Fe(C_{11}H_{19}O_2)_3$ for Fe. To grant a stable reactivity, Zr precursor was kept at 170 °C, while Fe precursor was maintained at 115 °C. Ozone was used as oxidizing gas in the reaction process. The film growth was achieved by alternately introducing the reactants separated by N_2 inert gas purging pulses. The Fe concentration in ZrO_2:Fe films was tuned tailoring the Zr/Fe precursors pulsing ratio and the growth

temperature was maintained at 350 °C (details in Ref. 29). After the deposition, the films were annealed at 600 °C in N_2 flux for 60 s. The growth parameters were tuned in order to fix the thickness, $d = 19 \pm 1$ nm, and the doping concentration $x_{Fe} = 20\% \pm 3\%$ for the ZrO_2:Fe films. x_{Fe} was chosen in order to stabilize the tetragonal phase according to our theoretical results.

Film crystallinity was checked by x-ray diffraction (XRD) at fixed grazing incidence angle $\omega = 1^\circ$ and using Cu K_α ($\lambda = 0.154$ nm) monochromated and collimated x-ray beam (details in Ref. 30). Film uniform doping along its thickness was checked by time of flight secondary ion mass spectrometry (ToF-SIMS) depth profiling using an ION-TOF IV instrument, with 500 eV Cs^+ ions for sputtering and 25 keV Ga^+ ions for analysis. Secondary ions were collected in negative polarity and interlaced mode. Recorded intensities were normalized to ^{30}Si intensity in bulk silicon. The instrument depth resolution is below 1 nm.

To elucidate the Fe chemical state and concentration in ZrO_2:Fe films, x-ray photoemission (XPS) measurements were performed on a PHI 5600 instrument equipped with a monochromatic Al K_a x-ray source ($E = 1486.6$ eV) and a concentric hemispherical analyzer. The spectra were collected at a take-off angle of 45° and band-pass energy 11.50 eV. The instrument resolution is 0.5 eV.

III. FIRST-PRINCIPLES PREDICTIONS

A. $V_O^{\bullet\bullet}$ and structural properties

In the literature, ZrO_2:Fe has been studied as a candidate material for oxygen sensing applications because Fe^{+3} atoms, replacing Zr^{+4} atoms, are expected to induce oxygen vacancies for charge compensation.[16,17] Thus, as a first step, we consider the $V_O^{\bullet\bullet}$ formation energy:

$$\Delta E_1(x_{Fe},z) = \{E(Zr_{1-x}Fe_xO_2) - [E(Zr_{1-x}Fe_xO_{2-z}) + (z/2)\mu(O_2)]\}/z \quad (1)$$

at fixed $y_{V_O^{\bullet\bullet}/Fe} = z/x = 0.5$, i.e., for a charge compensated system. Here, we considered both the oxygen-rich condition [see Fig. 1(a), $\mu(O_2) = E(O_2)$ with $E(O_2)$ the total energy of an isolated oxygen molecule in its ground state] and the oxygen-poor condition [see Fig. 1(b), $\mu(O_2) = E(ZrO_2) - E(Zr)$]. The formation energy for ZrO_2:Fe is compared with the case of pure ZrO_2, $\Delta E_1(0,z)$ and ZrO_2:Y, $\Delta E_1(x_Y,z)$. To this end, we considered different $V_O^{\bullet\bullet}$ concentrations and, for each different $V_O^{\bullet\bullet}$ configuration. However, we found that $\Delta E(x,z)$ is mainly determined by the kind of dopant, while the influence of the other parameters is lower. In Fig. 1, the changes due of these parameters result in different values for each system. While the V_O formation energy is negative in ZrO_2:Y already in the oxygen-rich case, in ZrO_2:Fe films it is slightly positive, i.e., $\Delta E_1^{tetra} \approx 0.5$ eV, but ten times lower than in pure ZrO_2. Varying the chemical potential from the oxygen-rich to the oxygen-poor configuration, ΔE_1^{tetra} becomes negative, thus Fe favors the formation of $V_O^{\bullet\bullet}$.

The creation of oxygen vacancies induces disorder in the system (see also the inset in Fig. 6) thus the most symmetric phases are expected to be favored against the monoclinic phase. To evaluate this effect, in Fig. 2, we consider the energy difference $\Delta E_2(x)$ between the tetragonal and the monoclinic phases as a function of the doping concentration at fixed $y_{V_O^{\bullet\bullet}/X} = 0.5$. We look for the iron atomic percent x_{Fe}^C at which the tetragonal phase becomes favored.

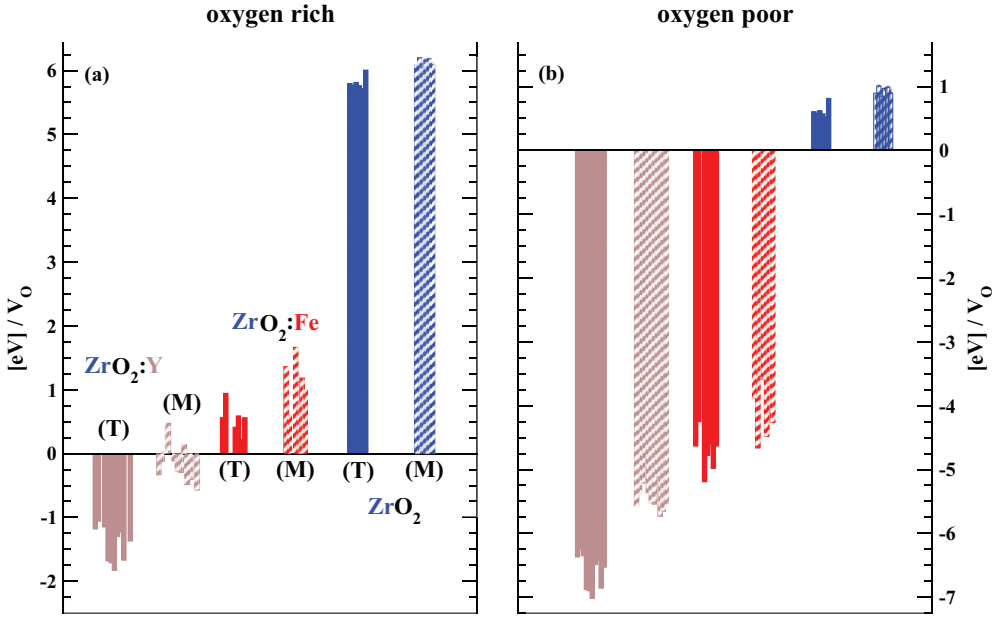

FIG. 1. (Color online) DFT (GGA) formation energy of oxygen vacancies [see Eq. (1)] in ZrO_2:Y, ZrO_2:Fe, and ZrO_2 in the two extrema case of (a) oxygen-rich and (b) oxygen-poor conditions in both the tetragonal and the monoclinic structures. The doped systems are considered in the charge compensated configuration (i.e., $y_{V_O^{\bullet\bullet}/X} = 0.5$ for $X = Fe, Y$). The values are computed for different oxygen vacancies concentrations and also varying, for some concentrations, the position of the oxygen vacancies. In (a) and (b), histograms are presented in the same order (and colors).

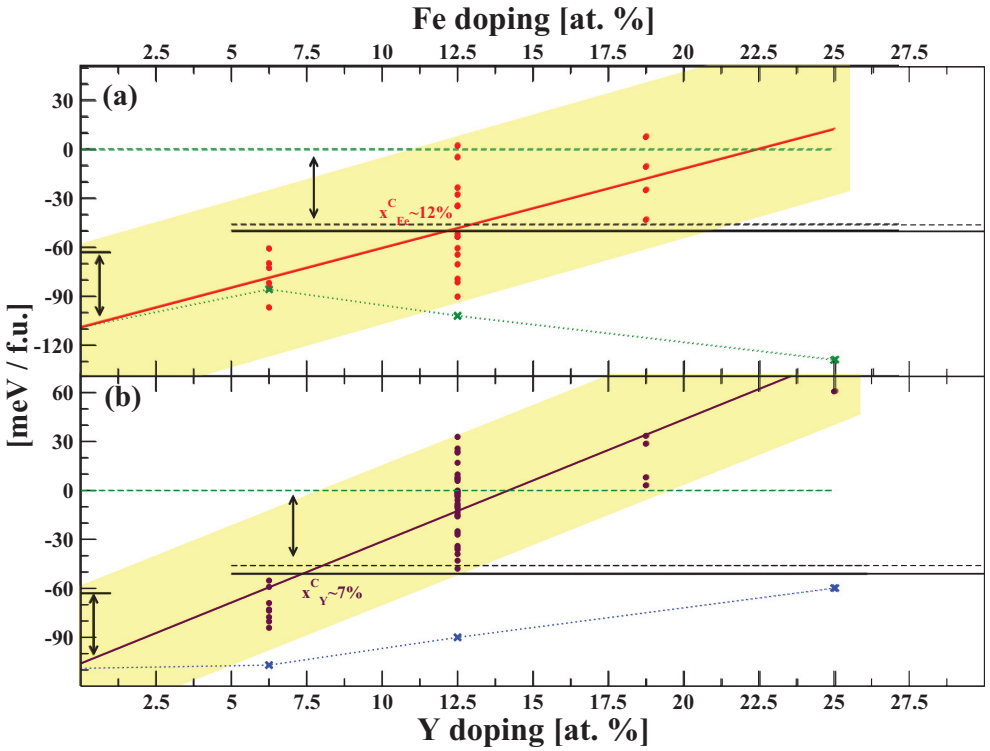

FIG. 2. (Color online) DFT (GGA) total energy difference per formula unit between the tetragonal against the monoclinic phase for (a) ZrO_2:Fe and (b) ZrO_2:Y. Total energies are computed for the charge compensated system (dots, $y_{V_O^{\bullet\bullet}/X} = 0.5$ for $X = \mathrm{Fe,Y}$) changing the atomic configurations for each given concentrations. The shadowed areas are guides for the eyes while the continuous lines are a linear fit of the data. Also the results for the systems without oxygen vacancies (crosses, $y_{V_O^{\bullet\bullet}/X} = 0$) are shown for comparison. The zero level is shifted by (i) -46 meV/f.u. to align the energy difference at zero doping with the experimental value, and (ii) -5 meV/f.u. to include the computed zero-point-energy difference of the two lattices.

The value of ΔE_2 is very small and thus at the limit of the DFT-GGA resolution. The computed energy difference between the two phases at zero doping is $\Delta E_2(0) = 109$ meV/f.u., in agreement with previous works (63 meV/f.u.,[20] 144 meV/f.u.[32]); the experimental estimation is 63 meV/f.u.[33] It is reasonable to assume that the trend of the energy difference is better computed than its absolute value and accordingly, assuming a constant "zero-doping error" of $\approx$46 meV/f.u. for every Fe concentration, we can subtract it. Being ΔE_2 of the order of few meV/f.u., also the phonon energy of the two lattices could play a role. Indeed, the monoclinic to tetragonal phase transition at $\approx$1440 K can be explained in this terms.[34,35] Thus we considered the energy difference of the lattice between the two structures for the undoped system. At room temperature, however, we found this contribution to be almost negligible, $\approx$5 meV/f.u.

ΔE_2 come out, instead, to be particularly sensitive to the chosen atomic configuration. Accordingly, the data in Fig. 2 are scattered, with ΔE_2 changing of few meV/f.u. at given x_{Fe}. To extract the exact x^C_{Fe}, a statistical occupation of the different configurations should be considered. However, to this end, one should sample a huge number of configurations, which is not feasible within DFT. In the present paper, we assumed that, for fixed x_{Fe} and $z_{V_O^{\bullet\bullet}}$, changing the configurations for the $V_O^{\bullet\bullet}$, ΔE_2 spans uniformly a given energy range (E_R), which can be extrapolated considering a limited number of configurations. E_R is expected to increase, increasing the doping concentration, as an increasing number of configurations becomes available. With these assumptions, x^C_{Fe} was extracted considering the central value of the E_R.

In practice, this was done with a linear fit of the data. In Fig. 2, to obtain the critical doping concentration, ΔE_2 at zero doping is matched at the experimental value 63 meV, while the theoretical results would be 109 meV. The result, $x^C_{\mathrm{Fe}} \approx 12\%$ at., can be compared with the case of ZrO_2:Y, where the same approach gives $x^C_Y \approx 7\%$ at., which exactly matches the experimental value.[31] We stress that with this approach the exact doping concentration can be affected by an error, which can be as large as few atomic percent. What is significant here is the comparison of the two systems, i.e., ZrO_2:Y and ZrO_2:Fe. Indeed, both dopants, inducing oxygen vacancies, favor the tetragonal against the monoclinic structure. However, the two linear fits posses different slopes and we can conclude that iron is less efficient than yttrium in inducing a monoclinic to tetragonal phase transition. In Fig. 2, we also report the energy difference between the monoclinic and the tetragonal phase for the case without oxygen vacancies, i.e., $y_{V_O^{\bullet\bullet}/X} = 0$. In this configuration, we found that the local structure of the crystal is much less distorted by doping and accordingly the variation of the energy difference between the two phases is small. This confirms that a key role in the monoclinic to tetragonal phase transition is played by oxygen vacancies[31] and not by the dopant itself.

B. Electronic properties

Given the results of the previous section and the fact that experimentally we describe a system at high doping concentration, which we found to be in the tetragonal phase, in the description of the electronic properties of the system, we focus our attention on the tetragonal structure of ZrO_2:Fe.

The main difference between Y and Fe is the presence of the unfilled Fe(d) orbitals, which, falling inside the energy gap of zirconia, determine the electronic properties of the doped system. The d-orbital occupation is also strongly affected by $V_O^{\bullet\bullet}$ and is used here, together with the computed magnetic moment, to infer the Fe oxidation state. At $y_{V_O^{\bullet\bullet}/\mathrm{Fe}} = 0$, Fe acts as an acceptor [see Fig. 3(a)] with the creation of holes in the majority spin VB. These are preferentially located on the Fe(d) orbitals as shown by the projected DOS with the projection of the hole states on the d orbitals close to 0.5. Thus Fe is forced in the Fe^{+4} oxidation state with a magnetic moment per atom equal to $4\mu_B$. The creation of $V_O^{\bullet\bullet}$ release the electrons captured by the O anions. At $y_{V_O^{\bullet\bullet}/\mathrm{Fe}} = 0.5$, the system turns into a charge-transfer semiconductor [see Fig. 3(b)], i.e., the $V_O^{\bullet\bullet}$ do not create impurity bands, as it would happen in ZrO_2, but compensate the holes in the Fe(d) orbitals. In this configuration, Fe atoms are in the +3 oxidation state and the magnetic moment per iron atom is maximized, $5\mu_B$. If $y_{V_O^{\bullet\bullet}/\mathrm{Fe}}$ exceeds 0.5, electrons start to fill the minority Fe(d) levels. This decreases the average magnetic moment, while the system reverts to a half-metal. At $y_{V_O^{\bullet\bullet}/\mathrm{Fe}} = 1$ [Fig. 3.(c)], all iron atoms are in a +2 oxidation state with the per atom magnetic moment equal to $4\mu_B$. In Fig. 3, we also notice that at $y_{V_O^{\bullet\bullet}/\mathrm{Fe}} \leqslant 0.5$ no extra state, other than the Fe(d) orbitals, appears between the valence and the conduction band of ZrO_2. Only when $y_{V_O^{\bullet\bullet}/\mathrm{Fe}} > 0.5$ [Fig. 3.(c)] such a state exists. The latter can be associated to an impurity band, which has been suggested to create bound magnetic polarons in case of magnetic doping.[3] However, the configuration $y_{V_O^{\bullet\bullet}/\mathrm{Fe}} = 1$ is not favored. Indeed, the energy cost for each extra $V_O^{\bullet\bullet}$ created in the system by the reaction

$$Zr_{1-x}O_{2-x/2}Fe_x \rightarrow Zr_{1-x}O_{2-x}Fe_x + \frac{x}{4}\mu[O_2] \qquad (2)$$

changes from ≈2.5 eV, oxygen-rich conditions, to ≈0 eV, oxygen-poor conditions, thus remaining positive for any value of the oxygen chemical potential. As for the $V_O^{\bullet\bullet}$ formation energy ΔE_1, this value is weakly dependent on the atomic doping x_{Fe}. Last but not least, even if in this case the impurity band exist, it is empty. Thus the possible existence of bound magnetic polarons in ZrO_2:Fe is unlikely. We will also show in the next section that, experimentally, iron in ZrO_2:Fe is in the Fe^{+3} and not in the Fe^{+2} oxidation state.

We remark that, even if at $y_{V_O^{\bullet\bullet}/\mathrm{Fe}} = 0$ and 1, the system is metallic, the per atom magnetic moment is integer. The reason is that in both cases ZrO_2:Fe is indeed a half-metal and thus electrons can move across the Fermi level only in one spin channel. We have verified this result increasing the sampling of the k-point grid from $2 \times 2 \times 2$ to $3 \times 3 \times 3$ in the 96 supercell and from $4 \times 4 \times 4$ to $8 \times 8 \times 8$ in the 12 atoms supercell. In both cases, the system remains metallic, with fractional occupation in the majority ($y_{V_O^{\bullet\bullet}/\mathrm{Fe}} = 0$) or minority ($y_{V_O^{\bullet\bullet}/\mathrm{Fe}} = 1$) spin channel (a smearing of 0.002 Ry was used in the self-consistent cycle in this case), but with constant per atom magnetic moment $m_z = 4\mu_B$. In principle, the 96 atoms supercell with a sampling $3 \times 3 \times 3$ is equivalent to the 12 atoms supercell with sampling $6 \times 6 \times 6$. However, the two could differ because in the 96 atoms supercell, by removing symmetries, disorder is taken into account. This could, for example, induce a complete localization of the holes on the Fe atoms. Thus the convergence check was also a rough way to explore possible Anderson-like localization mechanisms. However, we did not observe such phenomena.

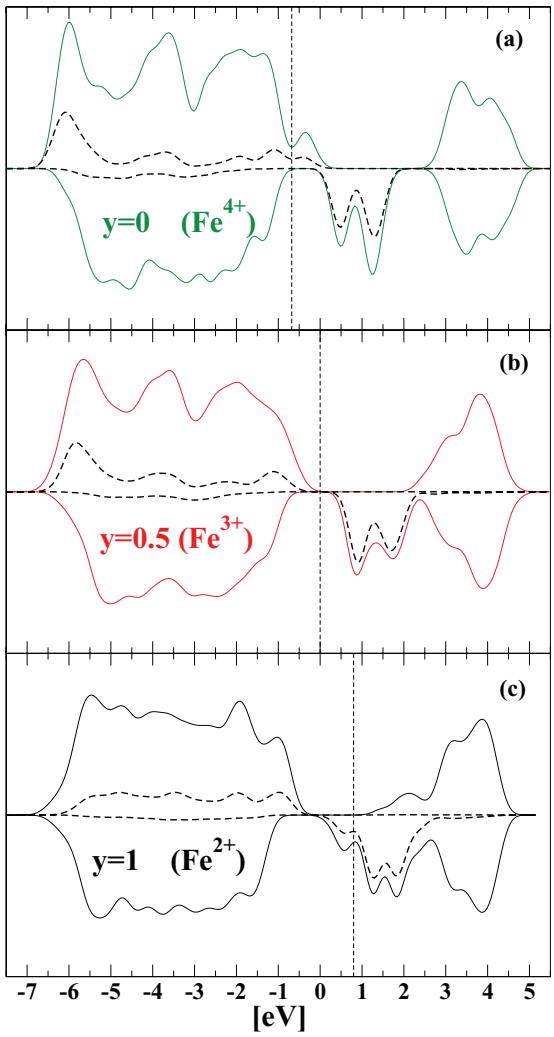

FIG. 3. (Color online) Total (full line) and d-orbital projected (dashed line) density of states (DOS) at the GGA level of ZrO_2:Fe at $x_{\mathrm{Fe}} = 25\%$ with $y_{V_O^{\bullet\bullet}/\mathrm{Fe}}$ equal to (a) 0, (b) 0.5, and (c) 1, respectively. The vertical dashed line marks the Fermi level. The Fermi level in (b) is the zero of the energy axis, while in (a) and (c), the zero is obtained aligning the bottom of the valence band at ≈−6.5 eV as in (b).

These are the predictions of the GGA. However, for TM oxides, this approximation is known to suffer of some deficiencies. In particular, it suffers of the well-known problem of self-interaction, which tends to delocalize too much the d orbitals. A common way to avoid this problem is to correct the DFT scheme with a Hubbard-like term U, which enters as an external parameter. The value of U is system dependent and should be optimized either with a direct comparison

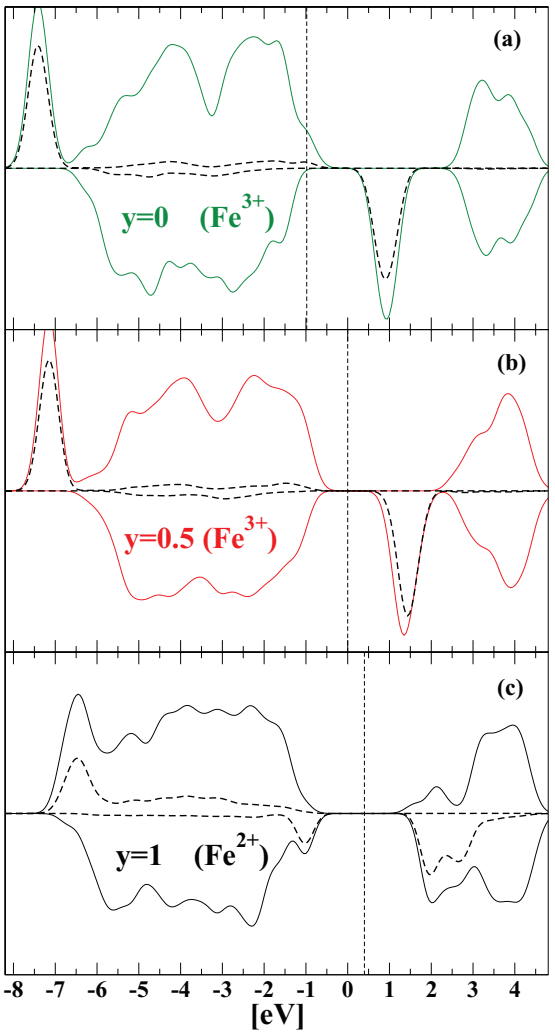

FIG. 4. (Color online) Total (full line) and d-orbital projected (dashed line) density of states (DOS) at the GGA + U level of ZrO_2:Fe at $x_{Fe} = 25\%$ with $y_{V_O^{\bullet\bullet}/Fe}$ equal to (a) 0, (b) 0.5, and (c) 1, respectively. The vertical dashed line marks the Fermi level. The Fermi level of (b) is the zero of the energy axis, while in (a) and (c), the zero is obtained by aligning the top of the conduction band at ≈5 eV as in (b).

with experimental data or with a self-consistent approach. In the literature, usually $U = 1-3$ eV for elemental iron and $U = 2-6$ eV in iron oxides. For example, Cococcini *et al.*[44] report, after a self-consistent calculation, $U \approx 2.2$ eV for metal iron and $U = 4.3$ eV for FeO. Here, we begin choosing an intermediate value, $U = 3.3$ eV, in order to evaluate the physical effects introduced by this correction.

In Fig. 4, we plot the DOS for the GGA + U approach at $y_{V_O^{\bullet\bullet}/Fe} = 0,\ 0.5,\ 1$. We can directly compare the results with the GGA DOS plots in Fig. 3. As expected, the U correction pushed down the occupied d level and a sharp structure appeared in the DOS just below the VB of ZrO_2:Fe. Also the crystal field splitting of the spin-minority d orbitals, between the e_g and the t_g states, was reduced and is not distinguishable anymore with the smearing parameter used in the plot; with the exception of the case $y_{V_O^{\bullet\bullet}/Fe} = 1$. However, in the charge-compensated situation, $y_{V_O^{\bullet\bullet}/Fe} = 0.5$, these corrections do not alter the qualitative description of the system, which remains a magnetic semiconductor with the magnetic moment per atom maximized. Instead, when we deviate from this configuration, we notice two important differences. For $y_{V_O^{\bullet\bullet}/Fe} < 0.5$, the holes created in the VB are less localized on the Fe atoms. Indeed, the projection of the hole states on the d levels drops from ≈0.5 (GGA) to less than 0.1 (GGA + U). Thus iron is in the Fe^{3+} configuration, while the holes are in the ZrO_2 VB, i.e., on the oxygen atoms. Accordingly, the $V_O^{\bullet\bullet}$ formation energy drops from 0.5 (GGA) to 0.0 eV because oxygen atoms are more weakly bound to the system. For $y_{V_O^{\bullet\bullet}/Fe} > 0.5$, the extra electrons start to fill the minority d levels, as in the GGA case. However, the newly occupied levels are pushed down in energy and thus the system is not metallic but it displays an energy gap, i.e., GGA + U predicts a a Mott insulator in this case. Also for the GGA + U case, we verified that in the metallic case (i.e., at $y_{V_O^{\bullet\bullet}/Fe} = 0$) the value of the magnetic moment remains constant improving the sampling of the Brillouin zone.

The electronic properties in the present section were reported for $x_{Fe} = 25\%$. We did not find significant changes for the other doping concentrations, at least for $y_{V_O^{\bullet\bullet}/Fe} = 0.5$. At the lowest computed doping concentration, however, $x_{Fe} = 6.25\%$, the Fe atoms are too far apart and the localized d levels do not create a band. Thus the metallic phases predicted within GGA ($y_{V_O^{\bullet\bullet}/Fe} = 0,\ 1$) become semiconducting phases with defect states localized close to the Fermi level.

IV. EXPERIMENTAL RESULTS

A. Structural characterization

Experimentally, as a first step, we first studied the structural properties of the film growth by atomic layer deposition. In Fig. 5, the ToF-SIMS depth profile of a representative film (namely, ZrO_2:Fe at $x_{Fe} = 20\%$ at.), including Fe, FeO, ZrO, and Si negative secondary ion intensity profile is graphed. Fe and FeO are both used as representative of Fe distribution along the film thickness; in particular, FeO ion fragment has

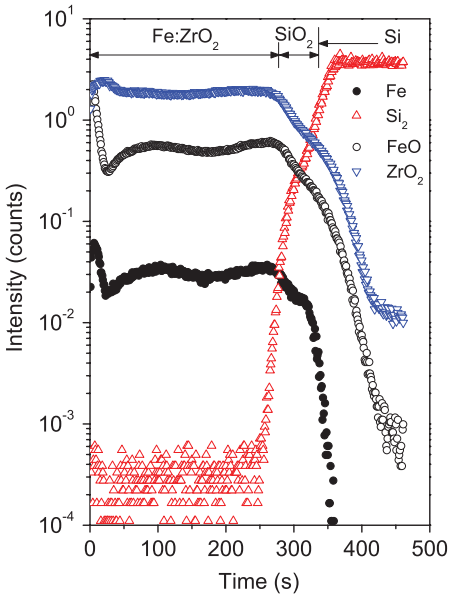

FIG. 5. (Color online) Tof–SIMS depth profile of ZrO_2:Fe at $x_{Fe} \approx 20\%$ *at*.

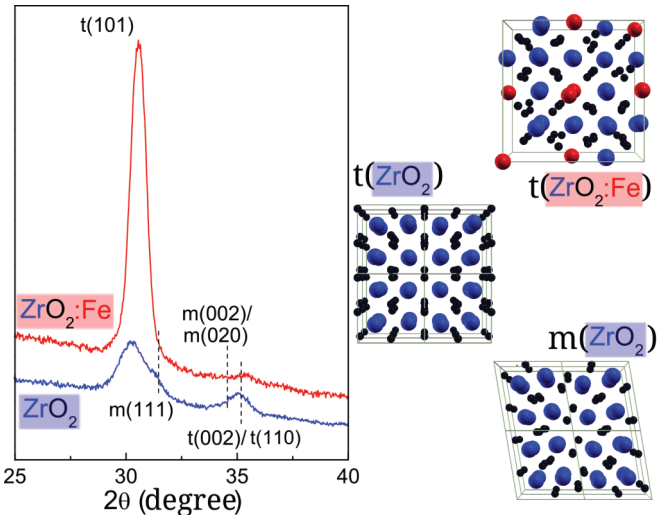

FIG. 6. (Color online) XRD patterns of ZrO_2 (blue) and ZrO_2:Fe (red) (Fe doping ≈20% at.) films evidencing Fe doping is effective in suppressing the monoclinic phase. t(ZrO_2) and m(ZrO_2) indicates the reflections from reference tetragonal and monoclinic ZrO_2, respectively.[38] (Right) Relaxed DFT structure for m(ZrO_2), t(ZrO_2), and t(ZrO_2:Fe) at $x_{Fe} = 25\%$ at. represented with the XCRYSDEN package (see Ref. 39); Zr atoms in blue, Fe atoms in red, and the smaller O atoms in black.

not to be considered as a mark of FeO chemical compound in the film, but as a fingerprint of Fe embedded in the ZrO_2 host matrix. The flatness of ZrO and Fe related profiles indicates that the film grows uniformly during the ALD process, without changes in the distribution of the chemical species, evidencing that the growth process is well controlled. Further, Si diffusion in ZrO_2 is excluded with a well distinct film/substrate interface, an indication that the substrate does not affect ZrO_2:Fe properties both during the film growth and the thermal treatment. Furthermore, the Fe profile is almost constant, thus it is the doping in the film, and the absence of large fluctuations such as peaked maxima, can exclude Fe clustering. Indeed, the latter would have been observed as a sudden increase of Fe intensity with a concomitant abrupt decrease of FeO intensity, indicating that an Fe-rich/O-poor environment is detected. Instead, both Fe and FeO signals mimic the same profile shape, confirming that Fe is uniformly diluted within the ZrO_2 matrix.

To get details on the film crystalline structure, in Fig. 6, we compare the XRD patterns of ZrO_2 and ZrO_2:Fe. Both films mainly present the cubic/tetragonal phase. Indeed, in these films, there is a balance between the bulk energy, where the monoclinic phase is favored, and the surface energy, where the tetragonal phase is favored. The critical grain size[36,37] below which the tetragonal phase becomes the most favored is ≈15 nm. In our films, being the grain size close to the film thickness (from XRD data), we are close to this critical value. This can be evinced from the XRD patterns of pure ZrO_2 where the peaks of the monoclinic phase are also evident. However, in the ZrO_2:Fe films, the monoclinic phase is completely suppressed, confirming our theoretical findings. Even from these measures there is no indication of segregated iron phase or iron oxide clusters.

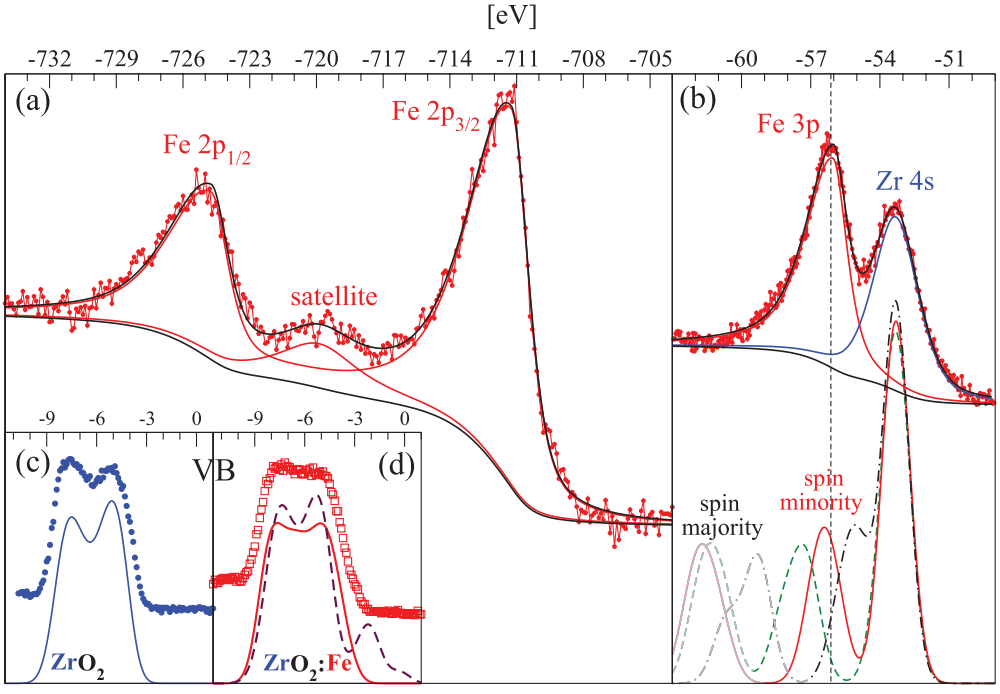

FIG. 7. (Color online) (a) The Fe($2p$) core level photoemission spectra in ZrO_2:Fe. (b) Fe($3p$) and Zr($4s$) photoemission spectra and computed DOS for ZrO_2:Fe with $y_{V_O^{\bullet\bullet}/Fe}$ equal to 0 (green dashed), 0.5 (red continuous), and 1 (black dot-dashed). The Fe($3p$) majority-spin level is in light gray. (c) Measured and computed valence band (VB) for pure ZrO_2. (d) Measured VB for ZrO_2:Fe. Computed VB for ZrO_2:Fe with Fe doping substitutional at $y_{V_O^{\bullet\bullet}/Fe} = 0.5$ (continuous red line) or interstitials (dashed maroon line). In (b)–(d), the experimental data (and fit) are vertically shifted with respect to the DFT-DOS. All DOS are obtained within the GGA. The experimental data were collected with the PHI 5600 instrument (see details in Sec. II B).

B. Electronic properties

In Fig. 7, we report the high-resolution spectra of the Fe($2p$) core level (a), the Fe($3p$) semicore (b) levels, and the VB (c) and (d). In Figs. 7(a) and 7(b), the data were fitted with a doublet of asymmetric Voigt functions for the two main peaks plus a Voigt function for the satellite on top of a Shirley background and in Figs. 7(b) and 7(d) the spectra are compared with DFT(GGA)-DOS computed as described in Sec. II A.

The change of the XPS-VB from ZrO_2 (blue) to ZrO_2:Fe (red) is in agreement with the DFT(GGA)-DOS obtained considering substitutional iron doping. In particular, experimentally the double peak structure of pure ZrO_2 is suppressed with doping. Theoretically, this behavior is reproduced only by assuming substitional doping.

The core or semicore levels of TM usually show a structured shape due to, at least, four factors: the spin-orbit (SO) splitting, the exchange splitting, the multiplet splitting, and the electron-hole screening to the core hole. The SO term is responsible for the $2p_{1/2}$–$2p_{3/2}$ splitting $\Delta E_{\mathrm{SO}} = 13.5$ eV and is not sensitive to the chemical environment [see Fig. 7(a)]. The exchange and multiplet splitting instead give the characteristic asymmetric shape of the XPS peaks in metals. Finally, the screening effect, which is strongly sensitive to the chemical environment,[40–42] can create satellites. For the Fe($2p$) core level, the distance between the satellite and the Fe($2p_{3/2}$) peak is a marker of the iron oxidation state.[43] Also the position of the Fe($3p$) peak [see Fig. 7(b)] is sensitive to the Fe chemical environment.[43] The comparison with the values of Ref. 43, reported in Table I, shows that iron is in the Fe^{+3} oxidation state.

According to our DFT results, the Fe oxidation state is strongly related to the presence of $V_{\mathrm{O}}^{\bullet\bullet}$ in the system (see Fig. 3). To better describe this point, we study the Fe($3p$) semicore levels with first-principles simulations. Indeed, the Fe($3p$) wave functions are spatially localized close to the Fe($3d$), which are in valence, and so are very sensitive to the chemical environment. The energy of the Zr($4s$) level is used as a reference to properly align the experimental XPS levels with the theoretical DOS.

In our approach, the SO coupling term was included both in the pseudopotentials and in the Hamiltonian, while the multiplet and the exchange splitting were accounted for by the exchange-correlation (xc) potential. For the Fe($3p$) level, we found $\Delta E_{\mathrm{SO}} \leqslant 1$ eV, while $\Delta E_{\mathrm{xc}} \approx 5$ eV between the spin minority and the spin majority, which is clearly visible in Fig. 7(b). This is overestimated by DFT. In the case of semicore levels, Takahashi *et al.*[41] showed that the screening effects, which are not included in the present approach, give a broadening and a shift of the majority-spin channel with, possibly, the creation of satellites. Indeed, we can suppose that these effects would correct the overestimated $\Delta E_{\mathrm{xc}} \approx 5$ eV, shifting the majority-spin energy level close to the minority one giving a single asymmetric peak with higher intensity as in the experimental case. However, such an approach is beyond the scope of the present work. The minority-spin channel instead is less affected by screening effects retaining the independent-particle structure with the onset of the spectrum due to absorption from this channel.[41] Thus we compared the energy position of the minority DOS with the measured Fe($3p$) XPS spectrum. In our simulations, the distance of the Fe($3p$) minority peak from the Zr($4s$) level, ΔE_y, is strongly dependent on $y_{V_{\mathrm{O}}^{\bullet\bullet}/\mathrm{Fe}}$ with $\Delta E_{y=0} = 1.8$, $\Delta E_{y=0.5} = 3.1$, and $\Delta E_{y=1} = 4.0$ eV. The value $\Delta E_{y=0.5}$, i.e., the configuration with iron in the Fe^{+3} oxidation state, best agrees with the experimentally measured splitting $\Delta E = 2.9$ eV, in agreement with the conclusion drawn from Table I and, in general, from Sec. III.

In Sec. III, we showed that the electronic properties and, in particular, the shape of the VB could be strongly influenced by the on-site electronic correlation, by the comparison of GGA and GGA + U predictions at $U = 3.3$ eV.

To decide which of the two scenarios, GGA or GGA + U, better describes the experimental situation we compared the obtained DOS for the charge-compensated case with the measured photoemission from the VB; the values $U =$ 0.0, 1.0, 2.0, 3.3 eV are here considered. To mimic the experimental spectrum, we have superimposed to the DFT-DOS a Shirley-like background, i.e., a background proportional to the integral of the DOS. Also, for a quantitative comparison, we computed the theoretical DOS for $y_{V_{\mathrm{O}}^{\bullet\bullet}/\mathrm{Fe}} = 0.5$ and $x_{\mathrm{Fe}} = 18.75\%$, which is the theoretical value closest to the experimental measured doping.

TABLE I. Energy distances (eV) from Fe($2p_{3/2}$). Data for iron oxides are from Ref. 43.

	Fe_2O_3	Fe_3O_4	FeO	ZrO_2:Fe
Fe($2p_{1/2}$)	− 13.6	− 13.5	− 13.6	− 13.5
Satellite	− 7.8	not present	− 6.0	− 8.6
Fe($3p$)	655.4	not available	653.9	655.2

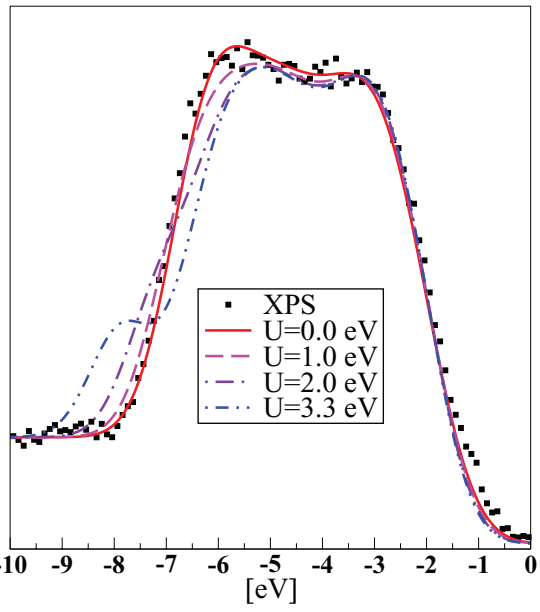

FIG. 8. (Color online) Valence band of ZrO_2:Fe. The GGA + U scheme at $x_{\mathrm{Fe}} = 18.75\%$, $y_{V_{\mathrm{O}}^{\bullet\bullet}/\mathrm{Fe}} = 0.5$, for the values of $U =$ 0.0, 1.0, 2.0, 3.3, is compared against experimental data. The smearing parameter used for the plot is 0.06 Ry. The experimental data were collected with the PHI 5600 instrument (see details in Sec. II B).

In Fig. 8, we see that the structure which identifies the d levels in the GGA + U, at the reference value $U = 3.3$ eV, is not present experimentally and the agreement between theory and experiment is much better in the standard GGA (i.e., $U =$ 0. eV). At the intermediate values $U = 1.0$ and 2.0 eV, such a structure is not visible, however, the agreement with the experimental results is worse than for the $U = 0$ eV case. We can conclude that the value $U = 0$ best agrees with the photoemission VB, and that, given the experimental resolution, the optimal choice of U must be between 0 and 1 eV. Thus, in ZrO_2:Fe, the effect of the self-interaction of the d orbitals, which is corrected by the Hubbard U term, is smaller than in common iron oxides. This is an *a posteriori* justification of the results obtained in the present work within the GGA.

V. CONCLUSIONS

In conclusion, we studied iron doped zirconia both theoretically with first-principles simulations and experimentally with structural, chemical, and electronic characterization of thin films grown by atomic layer deposition.

As expected from simple considerations, iron was found experimentally in the Fe^{+3} oxidation state. We also found that it induces a monoclinic to tetragonal phase transition. Theoretically, the oxidation state was related to presence of oxygen vacancies, which play a key role in the structural phase transition. The theoretical findings have been tested with a detailed comparison against photoemission spectra of the samples grown by atomic layer deposition to validate the assumptions. These results are a confirmation that iron doped zirconia could be a good candidate in view of oxygen sensing applications as reported in the past.

Moreover, the presence of vacancies is seen not only to influence the structure of the system but, theoretically, also to determine the density of states at the Fermi level and the eventual presence of impurity states in the gap, which could be associated to magnetic polarons. In particular, we discussed how the ratio between oxygen vacancies and the iron atoms concentration shifts the Fermi level of the system. We found that in the most stable configuration, the Fe^{+3} ions are charge compensated by the presence of oxygen vacancies with a ratio of 0.5, i.e., one vacancy for two iron atoms. The resulting system is a semiconductor with no impurity state in the gap.

These results should be considered for a correct description of the behavior of iron-doped zirconia, or more, in general, of high-k oxides doped with valence +3 elements, in resistive switching devices. Moreover, the absence of impurity states rules out the magnetic polaron model as a possible mechanism to explain the magnetic properties of the system.

Finally, we have explored the importance of the Hubbard U correction. Indeed, theoretically, varying the value of U from 0 to 3.3 eV, the electronic properties of the system change significantly. We showed that in iron-doped zirconia the value $U \approx 0$ eV best agrees with the experimental data, thus indicating that the on-site electronic correlation is low in this system.

ACKNOWLEDGMENTS

This work was funded by the Cariplo Fundation through the OSEA project 2009-2552. D.S. and A.D. would like to acknowledge G. Onida and the ETSF Milan node for the opportunity of running simulations on the "etsfmi cluster", P. Salvestrini for technical support on the cluster, and A. Molle and S. Spiga for useful comments and discussions. We also acknowledge computational resources provided under the project MOSE by CASPUR.

[1] H. Ohno, H. Munekata, T. Penney, S. von Molnar, and L. L. Chang, Phys. Rev. Lett. **68**, 2664 (1992).
[2] H. Ohno, A. Shen, F. Matsukura, A. Oiwa, A. Endo, S. Katsumoto, and Y. Iye, Appl. Phys. Lett. **69**, 363 (1996).
[3] J. M. D. Coey, M. Venkatesan, and C. B. Fitzgerald, Nat. Mater. **4**, 173 (2005).
[4] K. Sato, L. Bergqvist, J. Kudrnovsky, P. H. Dederichs, O. Eriksson, I. Turek, B. Sanyal, G. Bouzerar, H. Katayama-Yoshida, V. A. Dinh, T. Fukushima, H. Kizaki, and R. Zeller, Rev. Mod. Phys. **82**, 1633 (2010).
[5] H. P. Gunnlaugsson *et al*. (Isolde Collaboration), Appl. Phys. Lett. **97**, 142501 (2010).
[6] N. H. Hong, N. Poirotet, and J. Sakai, Appl. Phys. Lett. **89**, 042503 (2006).
[7] N. H. Hong, C.-K. Park, A. T. Raghavender, O. Ciftja, N. S. Bingham, M. H. Phan, and H. Srikanth, J. Appl. Phys. **111**, 07C302 (2012).
[8] N. H. Hong, J. Sakai, N. Poirot, and A. Ruyter, Appl. Phys. Lett. **86**, 242505 (2005).
[9] J. M. D. Coey, M. Venkatesan, P. Stamenov, C. B. Fitzgerald, and L. S. Dorneles, Phys. Rev. B **72**, 024450 (2005).
[10] V. V. Kriventsov, D. I. Kochubey, Y. V. Maximov, I. P. Suzdalev, M. V. Tsodikov, J. A. Navio, M. C. Hidalgo, and G. Colón, Nucl. Instrum. Methods Phys. Res., Sect. A **470**, 341 (2001).
[11] T. R. Sahoo, S. S. Manoharan, S. Kurian, and N. S. Gajhiye, Hyperfine Interact. **188**, 43 (2009).
[12] S. Ostanin, A. Ernst, L. M. Sandratskii, P. Bruno, M. Däne, I. D. Hughes, J. B. Staunton, W. Hergert, I. Mertig, and J. Kudrnovský, Phys. Rev. Lett. **98**, 016101 (2007).
[13] T. Archer, C. D. Pemmaraju, and S. Sanvito, J. Magn. Magn. Mater. **316**, e188 (2007).
[14] N. H. Hong, J. Sakai, N. T. Huong, N. Poirot, and A. Ruyter, Phys. Rev. B **72**, 045336 (2005).
[15] G. Stefanic, B. Grzeta, and S. Music, Mater. Chem. Phys. **65**, 216 (2000).
[16] W. Cao, O. K. Tan, W. Zhu, B. Jiang, and C. V. Gopal Reddy, Sens. Actuators B **77**, 421 (2001).
[17] W. Cao, O. K. Tan, J. S. Pan, W. Zhu, and C. V. Gopal Reddy, Mater. Chem. Phys. **75**, 67 (2002).
[18] H. Zhang, B. Gao, B. Sun, G. Chen, L. Zeng, L. Liu, X. Liu, J. Lu, R. Han, J. Kang, and B. Yu, Appl. Phys. Lett. **96**, 123502 (2010).

[19]S. Spiga, R. Rao, L. Lamagna, C. Wiemer, G. Congedo, A. Lamperti, A. Molle, M. Fanciulli, F. Palma, and F. Irrera, J. Appl. Phys. **112**, 014107 (2012).
[20]G. Stapper, M. Bernasconi, N. Nicoloso, and M. Parrinello, Phys. Rev. B **59**, 797 (1999).
[21]P. Giannozzi *et al*., J. Phys.: Condens. Matter **21**, 395502 (2009).
[22]J. P. Perdew, K. Burke, and M. Ernzerhof, Phys. Rev. Lett. **77**, 3865 (1996).
[23]P. Hohenberg and W. Kohn, Phys. Rev. **136**, B864 (1964).
[24]W. Kohn and L. J. Sham, Phys. Rev. **140**, A1133 (1965).
[25]D. Vanderbilt, Phys. Rev. B **41**, 7892R (1990).
[26]A. M. Rappe, K. M. Rabe, E. Kaxiras, and J. D. Joannopoulos, Phys. Rev. B **41**, 1227R (1990).
[27]C. Hartwigsen, S. Goedecker, and J. Hutter, Phys. Rev. B **58**, 3641 (1998).
[28]X. Gonze *et al*., Comput. Phys. Commun. **180**, 2582 (2009).
[29]A. Lamperti, E. Cianci, R. Ciprian, D. Sangalli, and A. Debernardi, Thin Solid Films (2012), doi:10.1016/j.tsf.2012.11.127.
[30]A. Lamperti, L. Lamagna, G. Congedo, and S. Spiga, J. Electrochem. Soc. **158**, G211 (2011).
[31]D. Sangalli and A. Debernardi, Phys. Rev. B **84**, 214113 (2011).
[32]J. K. Dewhurst and J. E. Lowther, Phys. Rev. B **57**, 741 (1998).
[33]R. J. Ackermann, E. G. Rauth, and C. A. Alexander, High. Temp. Sci. **7**, 304 (1975).
[34]A. Debernardi, C. Wiemer, and M. Fanciulli, Mater. Sci. Semicond. Process. **11**, 241 (2008).
[35]X. Luo, W. Zhou, S. V. Ushakov, A. Navrotsky, and A. A. Demkov, Phys. Rev. B **80**, 134119 (2009).
[36]A. Christensen and E. A. Carter, Phys. Rev. B **58**, 8050 (1998).
[37]G. Cerrato, S. Bordiga, S. Barbera, and C. Morterra, Surf. Sci. **377**, 50 (1997); Appl. Surf. Sci. **115**, 53 (1997).
[38]International crystal structure database, edited by FIZ Karlsruhe and NIST (2010). Code Nos. 68589 (t-ZrO_2) and 89426 (m-ZrO_2).
[39]A. Kokalj, Comput. Mater. Sci. **28**, 155 (2003).
[40]D.-J. Huang, D. M. Riffe, and J. L. Erskine, Phys. Rev. B **51**, 15170 (1995).
[41]M. Takahashi and J.-I. Igarashi, Phys. Rev. B **81**, 035118 (2010).
[42]A. K. See and L. E. Klebanoff, Phys. Rev. B **51**, 7901 (1995).
[43]T. Yamashita and P. Hayes, Appl. Surf. Sci. **254**, 2441 (2008).
[44]M. Cococcioni and S. de Gironcoli, Phys. Rev. B **71**, 035105 (2005).